This is a repository copy of *Low divergence single-mode surface-emitting concentric-circular-grating terahertz quantum cascade lasers*.

White Rose Research Online URL for this paper:
http://eprints.whiterose.ac.uk/78096/

Version: Published Version

**Article:**

# Low divergence single-mode surface-emitting concentric-circular-grating terahertz quantum cascade lasers

**Guozhen Liang,[1,7] Houkun Liang,[2] Ying Zhang,[2] Lianhe Li,[3] A. Giles Davies,[3] Edmund Linfield,[3] Siu Fung Yu,[4] Hui Chun Liu,[5] and Qi Jie Wang[1,6,7,*]**

[1]*NOVITAS, Nanoelectronics Centre of Excellence, School of Electrical and Electronic Engineering, Nanyang Technological University, 50 Nanyang Avenue, 639798 Singapore*
[2]*Singapore Institute of Manufacturing Technology, 71 Nanyang Drive, 638075 Singapore*
[3]*School of Electronic and Electrical Engineering, University of Leeds, Leeds LS2 9JT, UK*
[4]*Department of Applied Physics, Hong Kong Polytechnic University, Kowloon, Hong Kong*
[5]*Key Laboratory of Artificial Structures and Quantum Control, Department of Physics, Shanghai Jiao Tong University, Shanghai 200240, China*
[6]*Centre for Disruptive Photonic Technologies, School of Physical and Mathematical Sciences, Nanyang Technological University, 637371 Singapore*
[7]*CINTRA CNRS/NTU/THALES, UMI 3288, Research Techno Plaza, 50 Nanyang Drive, Border X Block, Level 6, 637553 Singapore*
[*]*qjwang@ntu.edu.sg*

**Abstract:** We report the design, fabrication and experimental characterization of surface-emitting terahertz (THz) frequency quantum cascade lasers (QCLs) with distributed feedback concentric-circular-gratings. Single-mode operation is achieved at 3.73 THz with a side-mode suppression ratio as high as ~30 dB. The device emits ~5 times the power of a ridge laser of similar dimensions, with little degradation in the maximum operation temperature. Two lobes are observed in the far-field emission pattern, each of which has a divergence angle as narrow as ~13.5° × 7°. We demonstrate that deformation of the device boundary, caused by anisotropic wet chemical etching is the cause of this double-lobed profile, rather than the expected ring-shaped pattern.

## References and links

1. M. Tonouchi, "Cutting-edge terahertz technology," Nat. Photonics **1**(2), 97–105 (2007).
2. R. Köhler, A. Tredicucci, F. Beltram, H. E. Beere, E. H. Linfield, A. G. Davies, D. A. Ritchie, R. C. Iotti, and F. Rossi, "Terahertz semiconductor-heterostructure laser," Nature **417**(6885), 156–159 (2002).
3. B. Williams, S. Kumar, Q. Hu, and J. Reno, "High-power terahertz quantum-cascade lasers," Electron. Lett. **42**(2), 18–19 (2006).
4. S. Fathololoumi, E. Dupont, C. W. I. Chan, Z. R. Wasilewski, S. R. Laframboise, D. Ban, A. Mátyás, C. Jirauschek, Q. Hu, and H. C. Liu, "Terahertz quantum cascade lasers operating up to ~200 K with optimized oscillator strength and improved injection tunneling," Opt. Express **20**(4), 3866–3876 (2012).
5. A. Wei Min Lee, Q. Qin, S. Kumar, B. S. Williams, Q. Hu, and J. L. Reno, "High-power and high-temperature THz quantum-cascade lasers based on lens-coupled metal-metal waveguides," Opt. Lett. **32**(19), 2840–2842 (2007).
6. M. Amanti, M. Fischer, C. Walther, G. Scalari, and J. Faist, "Horn antennas for terahertz quantum cascade lasers," Electron. Lett. **43**(10), 125–126 (2007).
7. W. Maineult, P. Gellie, A. Andronico, P. Filloux, G. Leo, C. Sirtori, S. Barbieri, E. Peytavit, T. Akalin, J.-F. Lampin, H. E. Beere, and D. A. Ritchie, "Metal-metal terahertz quantum cascade laser with micro-transverse-electromagnetic-horn antenna," Appl. Phys. Lett. **93**(18), 183508 (2008).
8. N. Yu, Q. J. Wang, M. A. Kats, J. A. Fan, S. P. Khanna, L. Li, A. G. Davies, E. H. Linfield, and F. Capasso, "Designer spoof surface plasmon structures collimate terahertz laser beams," Nat. Mater. **9**(9), 730–735 (2010).
9. N. Yu, Q. Wang, and F. Capasso, "Beam engineering of quantum cascade lasers," Laser Photonics Rev. **6**(1), 24–46 (2012).
10. M. I. Amanti, M. Fischer, G. Scalari, M. Beck, and J. Faist, "Low-divergence single-mode terahertz quantum cascade laser," Nat. Photonics **3**(10), 586–590 (2009).

11. S. Kumar, B. S. Williams, Q. Qin, A. W. Lee, Q. Hu, and J. L. Reno, "Surface-emitting distributed feedback terahertz quantum-cascade lasers in metal-metal waveguides," Opt. Express **15**(1), 113–128 (2007).
12. J. A. Fan, M. A. Belkin, F. Capasso, S. Khanna, M. Lachab, A. G. Davies, and E. H. Linfield, "Surface emitting terahertz quantum cascade laser with a double-metal waveguide," Opt. Express **14**(24), 11672–11680 (2006).
13. L. Mahler, M. I. Amanti, C. Walther, A. Tredicucci, F. Beltram, J. Faist, H. E. Beere, and D. A. Ritchie, "Distributed feedback ring resonators for vertically emitting terahertz quantum cascade lasers," Opt. Express **17**(15), 13031–13039 (2009).
14. E. Mujagić, C. Deutsch, H. Detz, P. Klang, M. Nobile, A. M. Andrews, W. Schrenk, K. Unterrainer, and G. Strasser, "Vertically emitting terahertz quantum cascade ring lasers," Appl. Phys. Lett. **95**(1), 011120 (2009).
15. Y. Chassagneux, R. Colombelli, W. Maineult, S. Barbieri, H. E. Beere, D. A. Ritchie, S. P. Khanna, E. H. Linfield, and A. G. Davies, "Electrically pumped photonic-crystal terahertz lasers controlled by boundary conditions," Nature **457**(7226), 174–178 (2009).
16. Y. Chassagneux, R. Colombelli, W. Maineults, S. Barbieri, S. P. Khanna, E. H. Linfield, and A. G. Davies, "Predictable surface emission patterns in terahertz photonic-crystal quantum cascade lasers," Opt. Express **17**(12), 9491–9502 (2009).
17. Y. Chassagneux, R. Colombelli, W. Maineult, S. Barbieri, S. P. Khanna, E. H. Linfield, and A. G. Davies, "Graded photonic crystal terahertz quantum cascade lasers," Appl. Phys. Lett. **96**(3), 031104 (2010).
18. G. Liang, H. Liang, Y. Zhang, S. P. Khanna, L. Li, A. Giles Davies, E. Linfield, D. Fatt Lim, C. Seng Tan, S. Fung Yu, H. C. Liu, and Q. J. Wang, "Single-mode surface-emitting concentric-circular-grating terahertz quantum cascade lasers," Appl. Phys. Lett. **102**(3), 031119 (2013).
19. J. Scheuer and A. Yariv, "Annular Bragg defect mode resonators," J. Opt. Soc. Am. B **20**(11), 2285–2291 (2003).
20. S. Kumar, Q. Hu, and J. L. Reno, "186 K operation of terahertz quantum-cascade lasers based on a diagonal design," Appl. Phys. Lett. **94**(13), 131105 (2009).
21. S.-H. Kim, S.-K. Kim, and Y.-H. Lee, "Vertical beaming of wavelength-scale photonic crystal resonators," Phys. Rev. B **73**(23), 235117 (2006).
22. N. Yu, L. Diehl, E. Cubukcu, D. Bour, S. Corzine, G. Höfler, A. K. Wojcik, K. B. Crozier, A. Belyanin, and F. Capasso, "Coherent coupling of multiple transverse modes in quantum cascade lasers," Phys. Rev. Lett. **102**(1), 013901 (2009).
23. A. K. Wójcik, N. Yu, F. Capasso, and A. Belyanin, "Nonlinear optical interactions of laser modes in quantum cascade lasers," J. Mod. Opt. **58**(9), 727–742 (2011).
24. W. Bewley, J. Lindle, I. Vurgaftman, J. R. Meyer, A. J. Evans, S. Slivken, M. Razeghi, C. S. Kim, and J. S. Yu, "Beam steering in high-power CW quantum-cascade lasers," IEEE J. Quantum Electron. **41**(6), 833–841 (2005).

## 1. Introduction

The terahertz (THz) frequency range, lying between microwave and mid-infrared frequencies (~0.3THz to 10THz), remains one of the least-developed regions in the electromagnetic spectrum. THz radiation has, however, proven and potential widespread and important applications in, for example, spectroscopy, heterodyne detection, imaging and communications [1]. In many of these applications, suitable high power coherent THz sources with low beam divergence and single-mode operation are highly desirable. Therefore, much effort has been placed on the development of new and appropriate THz sources, and in particular with a focus on the development of electrically pumped, semiconductor-based light sources that can be mass produced. A breakthrough occurred in 2002, when the first THz quantum cascade lasers (QCLs) was demonstrated [2].

QCLs are semiconductor lasers comprising multiple strongly coupled quantum wells, exploiting electron transitions between subbands in the conduction band. By adjusting the widths of the quantum wells/barriers, the emission frequency and performance of the laser can be tailored, adding additional flexibility in the laser design. THz QCLs can provide over 240 mW peak power in pulse mode, and 130 mW in continuous-wave (CW), at 10 K heatsink temperature, in devices using a single-plasmon waveguide [3]. Although this waveguide design gives high output power, the more recently developed metal-metal waveguide, where the THz QCL active region is sandwiched between two metal plates, enables a better temperature performance to be achieved (~200 K) [4]. However, owing to the subwavelength optical mode confinement of the metal-metal waveguide, conventional edge-emitting ridge THz QCLs are characterized by an extremely wide beam divergence (~180°), and a low output power, which is a result of a large impedance mismatch between the modes inside the cavity and in free space. Moreover, without a mechanism for mode-selection, ridge-waveguide lasers suffer from multiple-mode operation. These problems impede the practical applications of THz QCLs.

Various approaches have been developed to address these challenges, involving both edge-emitting and surface-emitting devices. For the former, early works employed additional optical components, such as silicon lenses [5] and horn antennas [6,7] to collimate the divergent output beam. These solutions are not easily integrated with the laser and require careful alignment, but Yu *et al.* subsequently developed an integrated spoof surface plasmon collimator for THz QCLs, and successfully reduced the beam divergence to ~10° [8,9]. None of these techniques provide optical mode selection, only optical collimation and beam engineering. However, in 2009, Amanti *et al.* showed that a third-order distributed feedback (DFB) grating could simultaneously enable single-mode operation and collimate the edge-emitting beam tightly (~10°) [10]. For surface-emitting devices, linear second-order DFB grating THz QCLs have been demonstrated to couple the optical power vertically out of a laser cavity [11,12]. However, although the beam divergence is narrow along the direction parallel to the ridge axis, it is still highly divergent perpendicular to the ridge axis. Therefore, to achieve a narrow and symmetric far-field profile in two dimensions, some researchers tried bending the laser ridges into rings, resulting in second-order DFB ring-grating THz QCLs [13,14]. However, the reported far-field patterns of these structures remained distorted. As an alternative approach, two-dimensional (2D) photonic crystals were investigated for controlling the surface emission from THz QCLs [15–17]. This allows the far-field profile to be engineered and provides controllable emission properties, and a large emission area. Indeed, single-mode devices with a range of far-field patterns have been reported, and beam divergences as low as ~12° × 8° have been obtained [17]. Nevertheless, it is not simple to achieve single-mode operation with these photonic crystal cavities because the design usually relies on the band structure of a unit cell of the photonic crystal with periodic boundary conditions, without considering the actual finite scale of the device. Moreover, it is not easy to predict and control the radiation loss (power) of the device without 3D full-wave simulations of the whole structure, which are often computationally intensive. Recently, we have demonstrated that through the use of second-order concentric-circular gratings (CCGs), one can realize surface-emitting THz QCLs with a side-mode-suppression-ratio of 30 dB and efficient power output, with little degradation in the maximum temperature performance [18]. The design of such CCGs is much easier than photonic crystal cavity structures, as it is possible to take advantage of the circular symmetry.

In this letter, we present the detailed design, fabrication and experimental results of THz frequency CCG DFB QCLs. Robust single-mode operation is realized at all bias currents, and the side-mode suppression ratios were as high as ~30 dB, indicating efficient single-mode selection. Moreover, the maximum operation temperature of 110 K is comparable with that of a ridge laser of similar size (130K), despite the output power of the CCG QCLs being ~5 times higher. The measured far-field pattern comprises two small lobes, both of which are within a 13.5° × 7° angular range. The deviation of the far-field pattern from the expected ring shape is attributed to deformation of the active region boundary due to the anisotropic wet chemical etching during fabrication.

## 2. Grating design

Our scheme for implementing the second-order CCG QCLs is shown in Fig. 1(a), where the 10-μm-thick active region is sandwiched between the metallic CCGs on top and a metal plate on the bottom. Inside the active region, the electric-field profile can be approximately expressed as a superposition of Bessel functions of the first and second kind, $J_m$ and $Y_m$, respectively [19]:

$$E_z(r) = \left[ A(r) J_m(kr) + B(r) Y_m(kr) \right] e^{im\varphi} \tag{1}$$

where $A(r)$ and $B(r)$ are the slowly varying mode amplitudes, $k$ is the wavevector in the active region, $\varphi$ is the azimuthal coordinate, and m = 0, 1, 2, …, denotes the order of the Bessel functions and also the order of the azimuthal modes.

The design of the structure was undertaken through numerical simulations using a commercial finite element method solver: *Comsol Multiphysics*. This solver is very effective in finding the eigenfrequencies and mode distributions of a resonator, although three-dimensional (3D) full-wave simulations of the proposed structure are computationally intensive and thus it is impractical to perform 3D simulations throughout the design. However, we can take advantage of the mode's known azimuthal dependence ($e^{im\varphi}$) and simplify the problem to a 2D cross-section simulation, as shown in Fig. 1(b); the magnified views show the widths of the metal in each period and the boundary region without metal coverage, denoted as $R_1$, $R_2$, … and $\delta$, respectively. Using the 2D "PDE (partial differential equation) Mode" of the *Comsol Multiphysics*, which allow the simulation based on user's own equations, one is able to calculate the optical modes with arbitrary azimuthal order (m) by solving the following equations:

$$\nabla \times \left( \epsilon^{-1} \nabla \times \overrightarrow{H} \right) - \omega^2 c^{-2} \overrightarrow{H} = 0 \qquad (2)$$

$$\overrightarrow{H}(r, z, \varphi) = \overrightarrow{H}(r, z) e^{-im\varphi} \qquad (3)$$

where $\overrightarrow{H}$ is the magnetic field, $\epsilon$ the relative permittivity, $c$ the speed of light in vacuum and $\omega$ the angular frequency of the light. Without lost of generality, we restrict our design to m = 0 (the fundamental azimuthal mode) because the surface-emitting beams of these modes give radial polarization, which is highly desirable when coupling light into a THz metal-wire waveguide or the metallic tip of a near-field imaging system.

The structure was designed to operate at ~3.75 THz. At this frequency, the real part of the refractive index of the active region was calculated to be ~3.6, from the emission spectra of a ridge laser with the same active region, using $n_{active} = c / (2L\Delta f)$, with $L$ being the length of the laser ridge and $\Delta f$ the Fabry-Pérot mode spacing in the spectra. To calculate the emission loss only, the imaginary part of the refractive index of the active region was set to zero and the metal was considered to be perfect. The 2D structure was then surrounded by an absorbing boundary that can isotropically absorb the emitted radiation without reflection.
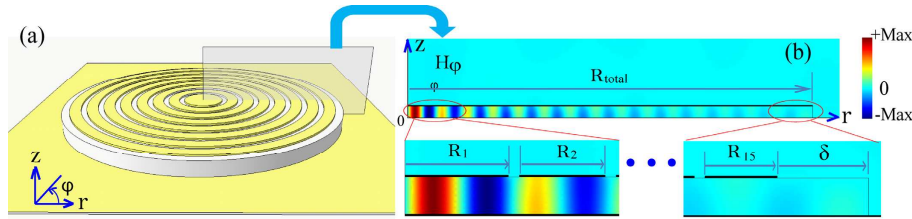


Fig. 1. (a) Three-dimensional schematic representation of the THz concentric-circular-grating quantum cascade laser design. The semitransparent rectangle represents the two-dimensional (2D) simulation plane. (b) 2D simulated magnetic field distribution making use of the 360°rotational symmetry of the designed structure. The magnified views show the widths of the metal in each period and the boundary region without metal coverage, indicated as $R_1$, $R_2$, … $R_{15}$ and $\delta$, respectively. The black lines represent metal.

The design began by determining the grating period and the widths of the open slits. For large area electric pumping via one or a few connected wires, it is important to guarantee uniform current injection over the pumping area, otherwise the mode behavior of the QCL may be disturbed. Therefore, the width of each open slits on the grating was predetermined as 2 µm. The effective refractive index of the CCG structure was then estimated to be $n_{eff}$ = 3.57, and so for a target wavelength of 80 µm (3.75 THz), a second-order grating period of 22.7 µm is required, which makes the mark-to-space ratio of the open slits less than 10%. We restricted the radius of the semiconductor active region $R_{total}$ to be ~16 grating periods, taking into account the maximum current output of commercial power supplies and the heat

extraction capacity of a typical cryostat. To suppress unwanted whispering-gallery-like modes, an annular boundary region of width $\delta = 22.7$ μm was left uncovered by metal [18].

The grating was initially designed as a standard second-order DFB grating. The whole grating structure starting from the center to the boundary is as follows: 20.7/**2**/20.7/**2**/20.7/**2**/20.7/**2**/20.7/**2**/20.7/**2**/20.7/**2**/20.7/**2**/20.7/**2**/20.7/**2**/20.7/**2**/20.7/**2**/20.7/**2**/22.7/**22.7** μm, where the bold number indicates the open region without metal coverage. The corresponding electromagnetic field distributions and spectra are shown in Figs. 2(a) and 2(b), respectively. A red arrow highlights the mode with the lowest loss, which is expected to be the lasing mode. However, since neighboring modes have similar predicted losses, this structure may not achieve single-mode operation. In linear DFB gratings, the width of the grating boundary plays a critical role in determining the mode behavior [11], and this also holds for our CCG design here. As shown in Figs. 2(c) and 2(d), by varying $R_{15}$ whilst keeping all other parameters unchanged, the corresponding mode spectrum changes significantly. The best result was achieved when $R_{15} = 16.2$ μm and correspondingly, $R_{total} = 356.7$ μm, as the expected lasing mode was most distinct from neigbouring ones. In the modifications that will be discussed below, $\delta$, $R_{15}$ and $R_{total}$ are left unchanged.

To exploit the gain of the active region fully, one should consider the electric field profile inside the cavity, with an evenly-distributed electric field profile being desirable. An uniform electric field distribution also helps improve the beam divergence. We thus investigated the $E_z$ (z-polarized electric field) profile inside the cavity, as the QCL active region can only provide gain for the TM mode (Figs. 2(e)–2(g)). For our initial designs, it can be seen that $E_z$ is concentrated in the central region (also shown in Fig. 2(a)). This is because the first few slits in the central region provide too strong feedback. In fact, the strength of feedback and the emission property of a slit depend critically on the location of the slit relative to the electric field: the slit provides the strongest feedback when placed at a null of the electric field, albeit with high emission loss from this slit. In contrast, a slit placed at an extremum of the electric field provides the weakest feedback and the lowest emitting loss. From Fig. 2(a) one can see that the first few slits are located near the nulls of the electric field, which explains their strong feedback and hence the high field concentration in the central region. To mitigate this, the positions of the first few slits were systematically adjusted to reduce their feedback.
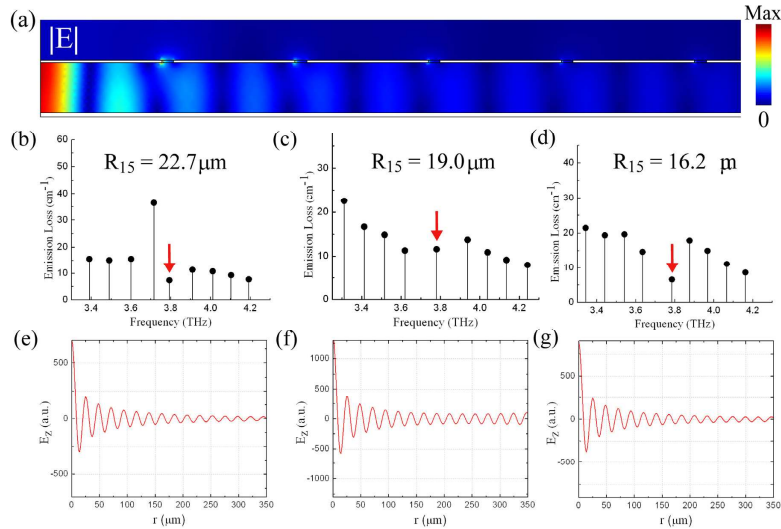


Fig. 2. (a) Electric field distribution of the standard second-order DFB CCG THz QCL in the central region. (b) – (d) Mode spectra of the structures for different $R_{15}$ with other parameters unchanged. (e) – (g) the corresponding electric-field ($E_z$) profiles of the expected modes, highlighted by the red arrows in (b) – (d), respectively, obtained at the middle height of the active region.

Figure 3 shows the simulated results following adjustment of slit locations. The slits are numbered outwards from the center as slit 1, 2, 3… . First, slits 1 and 2 were moved outwards by 3.4 μm; this aligned them with the maximum of the electric field (Fig. 3(a)(i)). $E_z$ thus becomes more evenly distributed along the radius (Fig. 3(a)(iii)), compared with Fig. 2(g), and the expected lasing mode is also more distinct from others (Fig. 3.(a)(ii)) because of the reduction in emission loss after this adjustment, as a result of the suppressed light emission from slits 1 and 2. To optimize the structure further, slit 3 was moved outwards by 1.9 μm (Fig. 3(b)), and then slits 4 and 5 were moved outwards by 0.7 μm (Fig. 3(c)). Figure 3(c) shows the final design. It has the greatest mode distinction, and most evenly-distributed $E_z$ field. Furthermore, the calculated emission loss is 3.9 cm$^{-1}$, comparable to that of a typical ridge THz QCL. The grating parameters starting from the center are: 24.1/**2**/20.7/**2**/19.2/**2**/19.5/**2**/20.7/**2**/20/**2**/20.7/**2**/20.7/**2**/20.7/**2**/20.7/**2**/20.7/**2**/20.7 /**2**/16.2/**22.7** μm, where the bold number indicates the open regions (slit or boundary region).
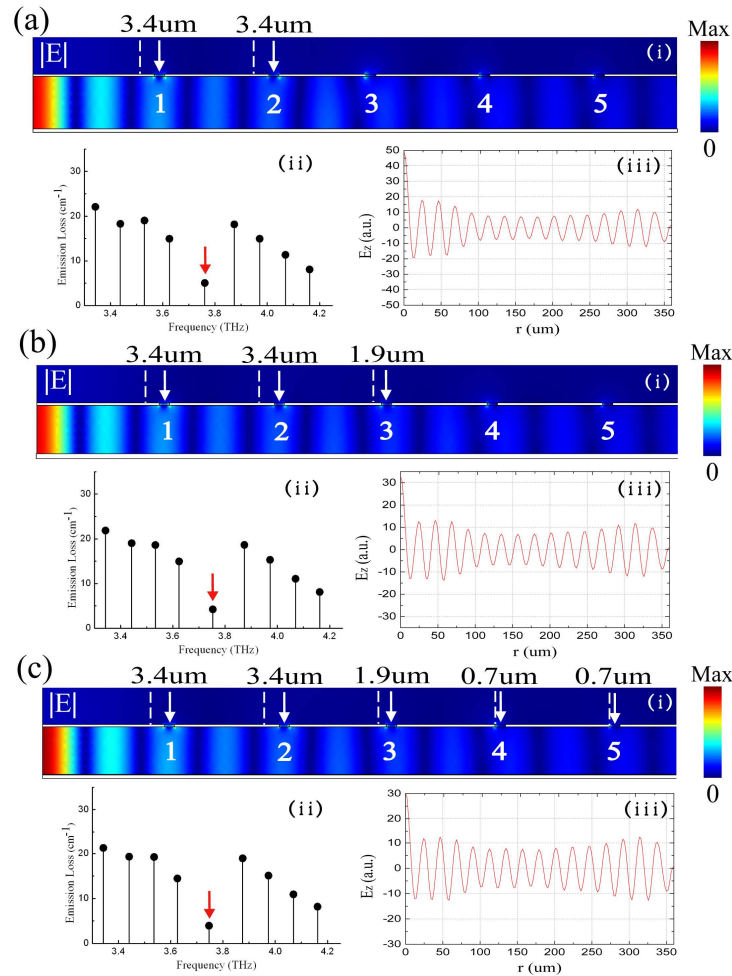


Fig. 3. (a), (b), (c) Simulation results after each adjustment of the slit locations. (i) Electric field (|E|) distribution of the expected mode at the central part of the grating. The first five slits are numbered 1, 2, …,5, and their locations are indicated by the white arrows. White dashed lines near the arrows indicate the original locations of the slits. The displacement distance of each slit is given above the arrow. (ii) Mode spectrum of the adjusted structure, a red arrow indicates the expected mode. (iii) The electric-field ($E_z$) profile.

Since the CCG is designed for an electrically-pumped QCL, a three-spoke bridge structure was employed to connect the concentric rings, as illustrated in Fig. 4(a), and to enable electric pumping of the whole grating.

The design discussed above considers only the fundamental azimuthal modes. However, higher azimuthal modes ($m \geq 1$) are also eigen-solutions of the circular structure, similar to the higher lateral modes in a ridge laser. To take into account these higher azimuthal modes and, more importantly, the influence of the three-spoke bridge, we performed a 3D full-wave simulation of the final structure. The computation took over 35 hours and 180 gigabytes RAM, running parallelly on a computing cluster node with 16 processes. Figure 4(b) presents the mode spectra of the first four azimuthal modes; modes $m > 4$ are not shown because they have higher loss. It can be seen that there usually exists a second-order azimuthal mode accompanying each fundamental mode with a similar loss. As the electric field in the active region can be described as a superposition of the Bessel functions of the first and second kind (Eq. (1)), we compare the fundamental ($J_0(r)$, $Y_0(r)$) and second-order ($J_2(r)$, $Y_2(r)$) Bessel functions in Figs. 4(c) and 4(d). From Fig. 4(c), we can see that the $-J_2(r)$ almost coincides with $J_0(r)$ except at the first two or three peaks, and the same is true for $-Y_2(r)$ and $Y_0(r)$ (Fig. 4(d)). Therefore, the CCG provides similar feedback and emission loss for the fundamental and second-order azimuthal modes, and hence the second-order azimuthal modes accompany the fundamental azimuthal modes, with similar emission losses. Nevertheless, the CCG is specifically optimized for the expected fundamental mode, and it consistently has a lower loss than the corresponding second-order mode. It should also be noted, from the inset of Fig. 4(b), that the perturbation of the three-spoke structure on the optical modes in the active region is minor.
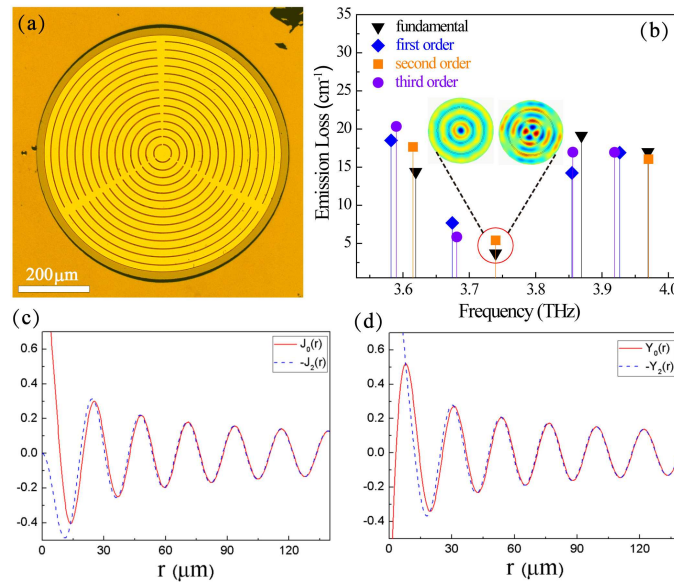


Fig. 4. (a) Optical microscope image of a fabricated CCG DFB THz QCL. A three-spoke bridge structure connects the concentric rings together to allow electrical pumping of the whole grating. (b) Mode spectrum of the device using 3D full-wave simulation to take the higher azimuthal modes into account. Only the first four lowest order azimuthal modes are plotted. The electric field distributions of the modes with lowest losses (the fundamental and second azimuthal modes, highlighted by a red circle) are shown in the inset. (c), (d) Comparison of the Bessel function $J_0(r)$ and $-J_2(r)$, and $Y_0(r)$ and $-Y_2(r)$, respectively. The fundamental and second-order Bessel functions coincide except in the first few peaks.

## 3. Fabrication and experimental results

The active region of the THz QCLs used for this work is a re-growth of that reported in Ref [20]. but with a slightly higher doping, whose heterogeneous GaAs/Al$_{0.15}$Ga$_{0.85}$As structure was grown on a semi-insulating GaAs substrate by molecular beam epitaxy. A Ti/Au (15/550 nm) layer was deposited on both the active wafer and a receptor n + GaAs wafer by electron-beam evaporation. The active wafer was inverted onto the receptor wafer, carefully aligning the crystal orientation of the wafer pair to facilitate cleaving. The wafer pairs were bonded together under application of pressure (~5.4 Mpa) at 300°C for 1 hour in a vacuum environment. The original substrate of the active wafer was then removed by lapping and selective chemical etching; this was followed by the removal of the highly absorptive contact layer of the active region using a H$_2$SO$_4$: H$_2$O$_2$: H$_2$O (1:7:80) solution, to prevent significant loss for the THz radiation coupled out through the grating slits. Top metal gratings (Ti/Au 15/200 nm) were defined by standard optical lithography and lift-off, after which the active region was wet-etched to form a disk structure using a H$_3$PO$_4$: H$_2$O$_2$: H$_2$O (1:1:10) solution with photoresist (AZ5214) used as the mask. The backside substrate was thinned down to ~150 μm to improve heat dissipation, and a Ti/Au (20/300 nm) layer was employed for the bottom contact. The sample was then cleaved, mounted onto Cu submounts, wire bonded, and finally put on the cold finger of a cryostat for measurement. Figure 4(a) shows the optical microscope image of a fabricated device.

Light-current-voltage (LIV) characterization was carried out at different heatsink temperatures under pulsed mode operation (200 ns pulses at 10 kHz repetition), and results are shown in Fig. 5(a). The devices operate up to 110 K. For comparison, the maximum operation temperature, under the same operation conditions, of double-metal waveguide, ridge lasers of similar size fabricated from the same epitaxial wafer is around 130 K. Figure 5(b) shows the emission spectra of the device at a 9 K heatsink temperature for various injection currents, ranging from threshold to the rollover. The detected side-mode suppression ratio (SMSR) is around 30 dB, limited by the noise floor of the room-temperature pyro-electronic detector, as shown in the inset to Fig. 5(b). This, together with the robust single-mode operation at 3.73 THz under all injected currents, reflects the strong single mode selectivity of the structure. Moreover, the collected power of the device is ~5 times higher than that of its ridge laser counterpart, indicating efficient light coupling out of the cavity by the grating.
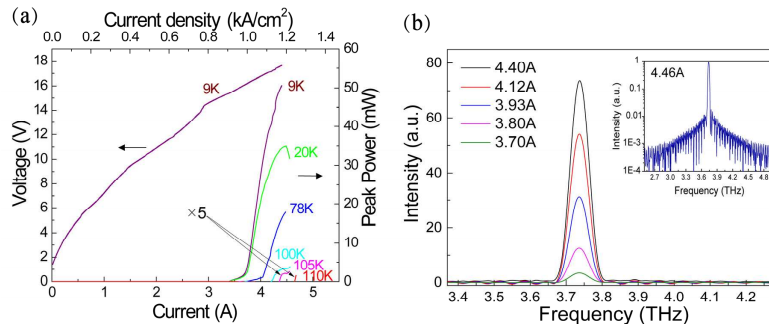


Fig. 5. (a) Light-current-voltage characterization of the CCG device at different heatsink temperatures under pulsed mode operation. (b) Emission spectra of the device at 9 K heatsink temperation as a function of injected current, from threshold to the rollover. The inset shows a logarithmic scale plot of the spectrum, demonstrating a side-mode suppression ratio of around 30 dB.

To investigate the electric field distribution in the grating cavity, the two-dimensional far-field emission pattern was measured. The radiation emitted by the device was sampled through a small aperture in front of a parabolic mirror, which was scanned over part of a spherical surface centered on the device. The parabolic mirror reflected the radiation into a liquid-helium cooled bolometer for detection. The small aperture was used to increase the

measurement angular resolution. The measured far-field pattern (Fig. 6(a)) exhibits double lobes, with full-width-at-half-maximum (FWHM) values of 13° × 6.5° and 13.5° × 7°. Similar results were obtained in several devices. This implies that the mode in the CCG resonator is not the expected fundamental mode, which should have a ring-shaped far-field pattern (Fig. 6(b)). Based on the method described in Ref [21], the calculated far-field profiles of the fundamental, the first-order and second-order azimuthal modes are shown in Figs. 6(b)–6(d), respectively; none has a double-lobe far-field profile.



Fig. 6. (a) Measured far-field pattern of a typical THz CCG QCL. (b), (c), and (d) Electric field distributions and the corresponding far-field patterns for the fundamental, the first-order and second-order azimuthal modes, respectively.

It was found that the deviation of the far-field pattern from the expected ring shape is due to an anisotropic sidewall profile caused by wet chemical etch. As shown in Fig. 7(a), the wet-etched sidewall is more vertical for the upper and lower boundaries than the left and right boundaries, which makes the shape of the disk slightly elliptical (the conjugate radius along the y-axis is 356.7 μm and the transverse radius along the x-axis is 358.7 μm). It should be noted that this deformation actually stems from the anisotropic crystal structure of the active region semiconductor, which makes the wet-etched sidewall profiles and the undercuts different along different crystallographic directions. Therefore, all the devices have similar, if not the same, boundary deformation. Although slight, this deformation breaks the circular symmetry of the fundamental mode (Fig. 7(b)) and consequently the simulated far-field pattern is as shown in Fig. 7(b), which agrees well with the measured result. It is worth mentioning that although the deformation of the boundary has such an effect on the fundamental azimuthal modes, the simulations show that there is negligible effect on the higher azimuthal modes. This is because higher order azimuthal modes have a lower degree of circular symmetry and are less sensitive to this deformation.

We've also considered the possibility that this far-field pattern might be due to the coherent superimposition of the fundamental and second-order azimuthal modes (Figs. 6(b) and 6(d)) since they're very close in the spectrum (Fig. 4(b)) and may not be discriminated in the measured laser spectra. If the phase difference of these two modes Δϕ is constant from pulse to pulse so that their far fields could be coherently superimposed during the measurement, the resulting far-field pattern may be double-lobed when their far-field electric fields have proper amplitudes and phases (Fig. 8(a)). Note that our devices worked in pulse mode operation, if Δϕ varies from one pulse to another, the measured far-field pattern of these two modes, if there are, will be resulted from their incoherent superimposition, which then is not double-lobed. However, even the best calculated result shown in Fig. R8(a) doesn't match well with the measured result (Fig. 6(a)). Furthermore, the mechanism that locks the phase difference of different modes is usually due to the nonlinear effects in the laser cavities, which requires high electric field intensity and, thus, may happen in high-power (watt level) lasers [22–24]. Since our devices are of relatively low power, it's unlikely that this nonlinear effect would play a role here. Moreover, when the injected current changes, this nonlinear

effect will change the value of Δφ and the amplitudes of these two modes significantly [22–24], leading to different far-field patterns, as shown in Fig. 8. However, in our measurement, the double-lobed far-field pattern didn't change when we changed the injected current. Therefore, with all these considered, it is unlikely that the double-lobed far-field patterns we measured are due to the superimposition of different azimuthal modes.
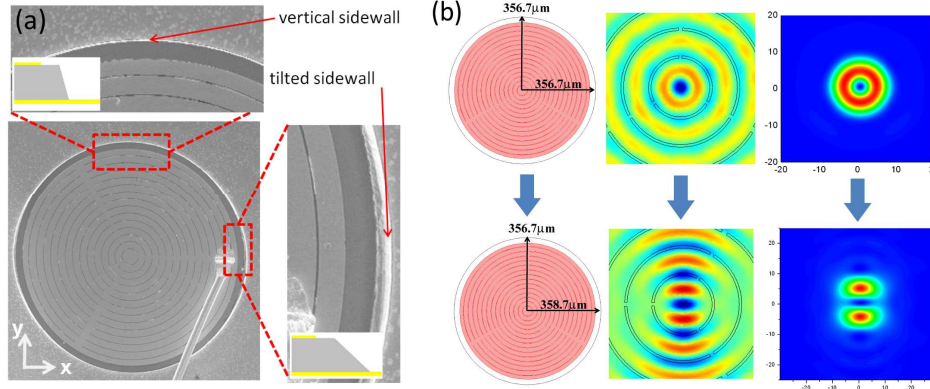


Fig. 7. (a) Scanning electron-beam microscope images of the anisotropic sidewall profiles caused by wet chemical etching. The sidewalls of the upper and lower boundaries are more vertical than those of the left and right boundaries. (b) The change of electric field distribution and far-field pattern caused by a slight (2 um) deformation of the circular active region disk.
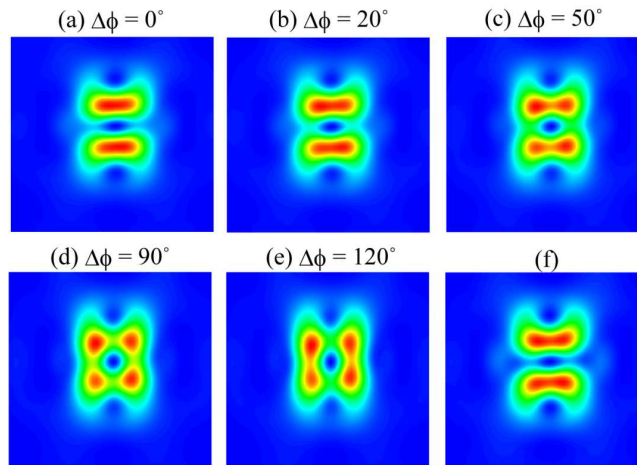


Fig. 8. Coherent superimposition of the far fields of the fundamental and second-order azimuthal modes. (a) – (e) Resulting far-field patterns with the phase difference of the two modes Δφ varies from 0° to 120°. (f) Resulting far-field pattern with Δφ = 0° but 1.5 times amplitude for the second-order azimuthal mode.

Another effect of the deformation is that it leads to frequency splitting of the original modes. As shown in Fig. 9, for the fundamental azimuthal mode, it will split into two deformed modes (Fig. 9 (b) and (c)) under the deformation, whose corresponding far-field patterns are shown in Fig. 9 (d) and (e), respectively. This is because, due to the deformation, the effective cavity length seen by these two modes are different, resulting in different eigen-frequencies and losses. However, in experiments, all the measured far-field patterns are similar as the one shown in Fig. 9(d), where the two lobes align in the perpendicular direction, indicating that only the mode shown in Fig. 9(b) is excited due to a lower loss.
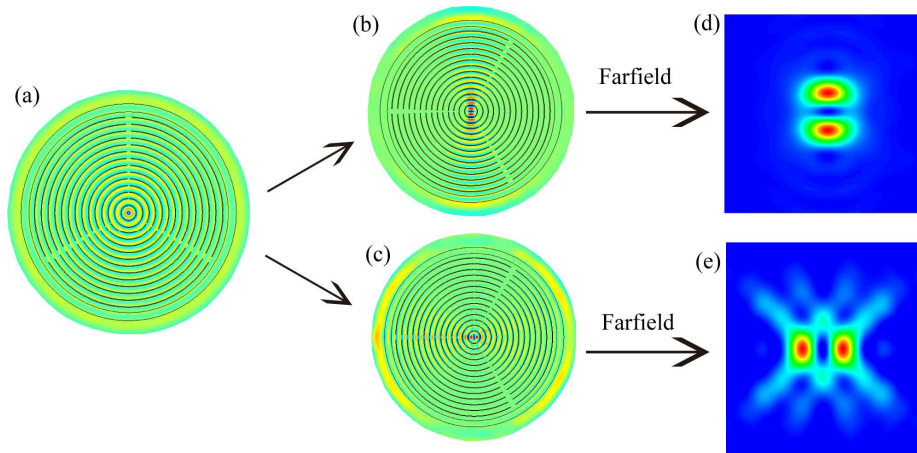
Fig. 9. Splitting of the fundamental azimuthal mode under deformation. (a) Electric field distribution of the original fundamental azimuthal mode. (b), (c) Electric field distributions of the splitted deformed fundamental azimuthal modes, and their corresponding far-field patterns (d), (e), respectively.

## 4. Conclusion

We have presented the design, fabrication and experimental measurements of surface emitting THz QCLs with second-order CCGs. Robust single-mode operation has been achieved with a SMSR as high as ~30 dB. Furthermore, the device emits ~5 times the power of a ridge laser of similar size, with little compromise in the maximum operation temperature. The beam divergence of the emitted radiation is greatly reduced, showing two small lobes in the far-field, each of which has a divergence angle within 13.5° × 7°, corresponding to the deformed fundamental azimuthal mode. The deviation of the far-field pattern from the expected ring shape is attributed to the boundary deformation of the active region, caused by the anisotropic wet chemical etching during fabrication.

## Acknowledgments